Applied Catalysis B: Environmental 279 (2020) 119398

Contents lists available at ScienceDirect

Applied Catalysis B: Environmental

journal homepage: www.elsevier.com/locate/apcatb

Interfacial electronic interaction of atomically dispersed $IrCl_x$ on ultrathin $Co(OH)_2$/CNTs for efficient electrocatalytic water oxidation

Yiwen Huang[a], Guijuan Wei[a], Jia He[a], Cuihua An[a], Min Hu[a], Miao Shu[b], Junfa Zhu[c], Shuang Yao[a,*], Wei Xi[a], Rui Si[b,*], Zhi-Ming Zhang[a], Changhua An[a,*]

[a] *Tianjin Key Laboratory of Organic Solar Cells and Photochemical Conversion, School of Chemistry and Chemical Engineering, Tianjin Key Laboratory of Advanced Functional Porous Materials, Institute for New Energy Materials & Low-Carbon Technologies, Tianjin University of Technology, Tianjin 300384, China*

[b] *Shanghai Synchrotron Radiation Facility, Shanghai Institute of Applied Physics, Chinese Academy of Sciences, Shanghai 201204, China*

[c] *National Synchrotron Radiation Laboratory, University of Science and Technology of China, Hefei, Anhui 230029, China*

ARTICLE INFO

Keywords:
Interfacial electronic interaction
Molecularly dispersed
Water oxidation

ABSTRACT

The exploration of highly-efficient oxygen evolution reaction (OER) electrocatalyst with well-defined structure to understand specific structure-performance relationship is crucial to meet the requirement of water-splitting. Herein, we firstly used atomically dispersed $IrCl_x$ to uniformly decorate ultrathin $Co(OH)_2$ nanosheets to dramatically improve electrocatalytic activity. The synthesized $IrCl_x$-$Co(OH)_2$ nanosheets/carbon nanotubes (CNTs) exhibits an overpotential of 230 mV to reach 10 mA/cm^2, which was much enhanced compared to that of pristine $Co(OH)_2$/CNTs (308 mV) and commercial benchmark IrO_2 (309 mV). X-ray absorption fine structure and density functional theory simulations demonstrate strong interfacial interaction between $IrCl_x$ and $Co(OH)_2$ nanosheets via the Cl-Ir-O and Ir-Cl-Co bond can efficiently boost its electronic conductivity. The accelerated charge transfer promotes the formation of more positively charged O atoms around cobalt centers, which is beneficial for the deprotonation on $IrCl_x$-$Co(OH)_2$ and makes the catalyst facilitate OER.

1. Introduction

The increasing consumption of fossil fuels and environmental problems stimulates the acceleration of exploring sustainable energy sources [1–5]. Electrocatalytic water splitting has been a potential strategy for the generation of new energy carriers [6,7]. In this process, the step of oxygen evolution reaction (OER) is critical to address increasing energy needs, which is limited by the sluggish kinetics and high overpotential [8–16]. Although IrO_2/RuO_2 based OER catalysts can realize comparable efficiency, their scarcity and high price greatly hamper extensive commercial applications. Presently, developing inexpensive and robust electrocatalysts as the alternatives to achieve high OER activity is highly desirable. Great progress has been made towards the exploration of non-noble metal OER catalysts, including various carbons, transition metal hydro(oxide)s, and others [17–20]. Among them, the low-cost Co and Ni hydroxides with proper electron configuration, tailorable chemical valence and versatile composition have received much attention to drive OER [21, 22]. However, these materials usually possess poor conductivity and low stability in strong alkaline electrolytes. Deposition of ultrathin Co and Ni hydroxides nanosheets on conductive carbon substrates has been as a robust way to overcome these problems [23, 24]. Atomic Iridium incorporated cobalt hydroxide with optimized 9.7 % Ir content was synthesized through a hydrothermal route, over which the realization of current density at 10 mA cm^{-2} requires an overpotential of 373 mV [25].

As well-known electronic structures of the catalysts play essential role in determining their performances [26–28]. Interfacial engineering represents a robust and effective strategy in terms of engineering surface electronic features of the electrocatalysts [29, 30]. Manipulating the interface by incorporating single atomic/molecular components can construct advanced materials with well-defined structure to reveal and facilitate charge transfer between different components. In the several past decades, interfacial metal-support interactions (IMSI) have been widely studied in the heterogeneous catalysis [31–33], which greatly improves the performance of the catalysts with supported metal particles [34, 35]. In order to rule out the intrinsic metal effects, more and more attention has been paid on uniformly dispersing single-atom (or single-molecule) metal sites on the supports to deeply understand the contribution of the interface charge transfer and intrinsic reaction mechanism.

In this work, we develop an ambient temperature synthetic strategy to uniformly disperse single $IrCl_x$ on ultrathin $Co(OH)_2$ nanosheets/

---

* Corresponding authors.
E-mail addresses: shuangyao@tjut.edu.cn (S. Yao), sirui@sinap.ac.cn (R. Si), anch@tjut.edu.cn (C. An).

https://doi.org/10.1016/j.apcatb.2020.119398
Received 9 April 2020; Received in revised form 31 July 2020; Accepted 3 August 2020

carbon nanotubes (CNTs) hybrids, resulting in a series of single-molecule catalysts ($Co(OH)_2$/CNTs-IrCl-x) (x = 0, 0.05, 0.075, 0.15) by facilely adjusting the feeding amount of $IrCl_3$. Interfacial interaction between $Co(OH)_2$ nanosheets and $IrCl_x$ species makes the $IrCl_x$ firmly attach to the support via a main Cl-Ir-O bond and chlorine bridge bond of Ir-Cl-Co. Experimental investigations and DFT calculations demonstrate that strong interfacial interaction can efficiently boost their electronic conductivity to create more positively charged O atoms around cobalt centers. Thus, the Ir^{4+} centers attached to the $Co(OH)_2$ is beneficial for deprotonation on $IrCl_x$-$Co(OH)_2$ to facilitate OER. As a result, the atomic-dispersed catalyst of $Co(OH)_2$/CNTs-IrCl-0.075 exhibits excellent catalytic activity. The realization of 10 mA/cm^2 requires 230 mV overpotential, which was much enhanced compared to $Co(OH)_2$/CNTs (308 mV) and commercial IrO_2 (309 mV).

2. Materials and methods

2.1. Materials

$NH_3{\cdot}H_2O$, $CoCl_2{\cdot}6H_2O$, and C_2H_5OH were bought from MACKLIN. CNTs was purchased from XFNANO (the diameter is 30 − 50 nm, the length is 10 − 20 μm, respectively). $IrCl_3{\cdot}xH_2O$ and Nafion solution with a concentration of 5 wt% were bought from Aldrich Chemicals. $(CH_2OH)_2$ was from Aladdin Industrial Corporation.

2.2. $Co(OH)_2$/CNTs preparation

Nanosheets of $Co(OH)_2$ was synthesized following the modification of previous report [36]. Taken the $Co(OH)_2$/CNTs-2.5 as an example, 2.5 mg of CNTs and 0.4 mmol $CoCl_2{\cdot}6H_2O$ of were added into mixture of DI water (10 mL) and EG (30 mL) and stirred 30 min vigorously. Subsequently, 120 μL of ammonium hydroxide solution was injected and stirred 15 min additionally. The mixture was sealed into a Teflon-lined stainless-steel autoclave and maintained 24 h at 130 ℃. The obtained sample was being dried at 60 °C for 6 h.

2.3. $Co(OH)_2$/CNTs-IrCl preparation

In a typical loading Ir-Cl species on the $Co(OH)_2$/CNTs, 20 mg of the $Co(OH)_2$ nanosheets/CNTs was firstly dispersed in 10 mL of DI-water under ultrasonic vibration, aqueous solution of $IrCl_3{\cdot}xH_2O$ (10 mL, 0.47 M) was introduced slowly via a syringe pump. The obtained mixture was continuously stirred 6 h. The final samples were rinsed with DI-water and centrifuged for their collection. After being dried in vacuum oven, the samples were collected for further characterization and evaluation.

2.4. Structural characterizations

The chemical composition and structures of the samples were studied by powder X-ray diffraction (PXRD, Rigaku Ultimalv Cu Kα), X-ray photoelectronic spectra (XPS, AXIS Ultra DLD system), and inductively coupled plasma-mass spectrometry (ICP-MS, Thermo Fisher iCAPTM RQ series analyzer). The fine microstructures were studied on field emission scanning electronic microscope (SEM, FEI Verios 460 L), Transmission electronic microscope (TEM, FEI TalosF200X), and the high angle annular dark field scanning transmission electronic microscopy (FEI Titan Cubed Themis G2300, HAADF-STEM).

2.5. Electrochemical performance tests

All the evaluations were performed on a CHI760E electrochemical workstation (Shanghai Chenhua, China) with 3-electrode configuration system. The Glass carbon electrode was firstly polished with Al_2O_3 suspension (0.05 μm, ChangSha, XINHUI TECHNOLOGY, LTD) and thoroughly cleaned. The sonication of the mixture of 5 mg catalyst, 450 μL of ethanol and 50 μL 5 wt% Nafion solution results in the formation of ink of catalyst. Then 5 μL of the dispersion was dropped onto the GC electrode and being dried naturally in air. The catalyst ink coated GC electrode was used as working electrode, a carbon rod was the counter electrode, and Hg/HgO electrode was the reference electrode, respectively. All the obtained potentials vs Hg/HgO electrode can be normalized on the basis of reversible hydrogen electrode (RHE) scale with Nernst equation: $E_{RHE} = E_{Hg/Hgo} + 0.059 \times pH + 0.9254$ (pH = 14 for 1 M KOH). The overpotential (η) was estimated by equation of $\eta = E_{RHE} - 1.23$. Before the linear sweep voltammetry (LSV) initiated, the catalyst should be carried out a mountain of CV cycles so as to obtain stable CV curves. The LSVs and CVs were scanned at a rate of 10 mV^{-1} without iR-compensation. The stability test was checked with amperometric measurement at 1.475 V. Tafel plots were obtained according to $\eta = b \log j + a$ from LSV curves, in which b, j separately represents the Tafel slope and current density. The electrochemical active surface areas were calculated by CV tests from 1.17 V to 1.27 V versus RHE with scan rates in a range of 10 − 50 mV s^{-1}. The double layer capacitance (C_{dl}) was derived from plotting the differences of charge current density ($\Delta j = j_{anodic} - j_{cathodic}$) at 1.22 V vs scan rate. The C_{dl} value is half of the fitting line slope.

2.6. Theoretical calculation

All the calculations are carried out using DMol3 code (Delley, 2000) through spin polarization density functional theory (DFT). The exchange correlation has been done by means of Perdew-Burke-Ernzerhof (PBE) parameterization of the generalized gradient approximation (GGA) [37]. The basis sets were double numerical plus polarization (DNP). Effective core potential (ECP) was used to process the inner electrons in the metal atoms, the other atoms were treated by all-electron basis set. The convergence criterion of $2*10^{-5}$ Ha was used for self-consistent field (SCF) calculation. For geometric optimization, the displacement and maximum force were 0.005 Å and 0.004 Ha/Å, respectively. The cutoff radius of the real space global orbital was chosen as high as 4.5 Å. Brillouin zone was adopted by 3 × 3 × 1 sampling k-points, and the optimization of lattice constants was applied in different systems. In order to prevent interaction between periodic images, the vacuum space is set to at least 15 angstroms in z direction. The change of free energies on various surfaces is derived from the following formula: $\Delta G = \Delta E + \Delta ZPVE + \int CpdT - T\Delta S$, where E is the change of adsorption energy, ΔZPVE and ΔS represent the difference of zero-point vibrational energy and entropy between adsorption state and gas phase. Cp and T represent the heat capacity and the system temperature, respectively. DFT calculations were used to predict thermodynamic characteristics of gas molecules. Following the previous theoretical results, ZPE contribution in the free energy expression was derived from the vibrational frequencies of adsorbed species [38, 39].

The XAFS measurements at Ir L_3 (E_0 = 11215.0 eV) edge were done at BL14W1 beamline of Shanghai Synchrotron Radiation Facility (SSRF), and operated at 3.5 GeV with “top-up” mode under 250 mA. The data were collected with a solid state detector of 32-element Ge using fluorescence mode. The absorption edge on Ir foil was applied to calibrate. The data were extracted and fit by Athena and Artemis codes in IFEFFIT software packages. For XANES, background subtraction and normalization were used to process the absorption coefficients vs function of energies $\mu(E)$, and assigned as “normalized absorption” with E_0 = 11215.0 eV over the sample and IrO_2/Ir foil. The molar fraction of Ir^{4+}/Ir° was estimated from the linear combination fit [40] by referring Ir foil and IrO_2. In the case of EXAFS, first-shell approximate model of Ir-O and Ir-Cl contributions were applied to analyze the Fourier transformed (FT) data in R space. Fitting the experimental data of Ir foils with the coordination number (CN) of Ir-Ir to fix 12 was used to calculate the passive electron factors, $S_0{}^2$, which was then assigned for their analyses. The parameters for the description of the electronic properties,*i.e.*, correction to the photoelectron energy origin, E_0, local

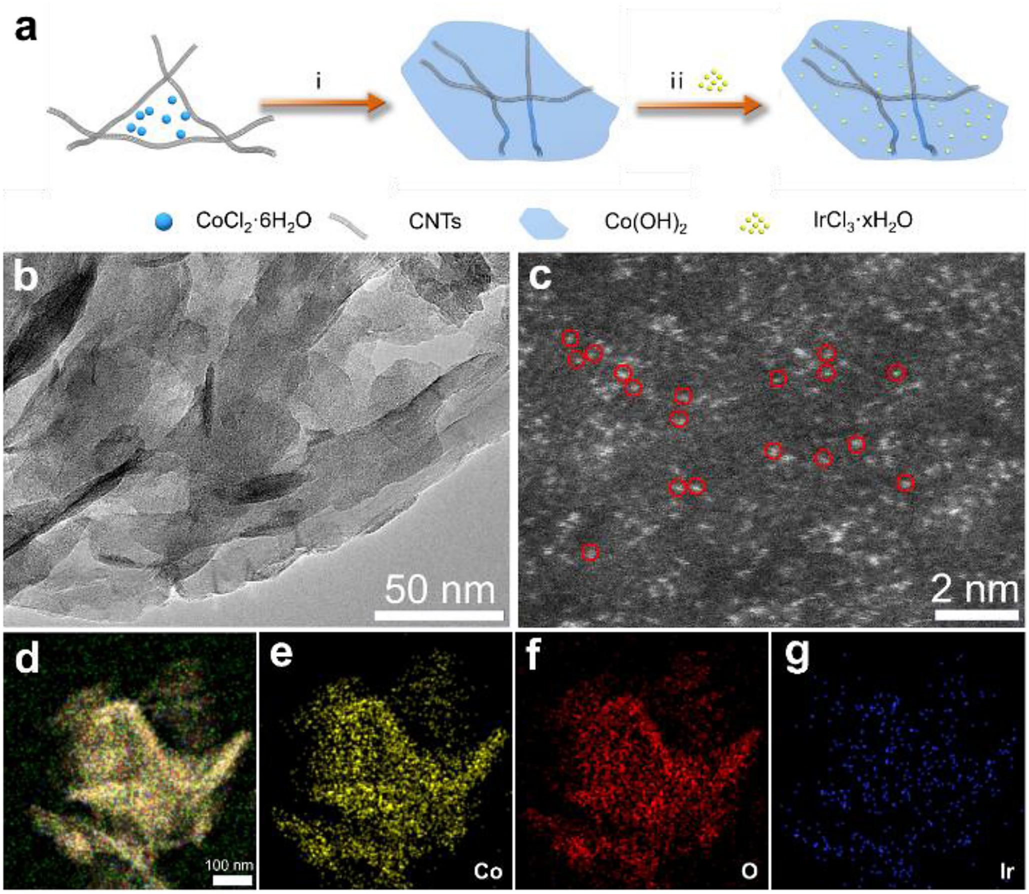

Fig. 1. a) Typical synthetic scheme of the single-molecule catalysts. b) A TEM image of $Co(OH)_2$ nanosheets/CNTs-IrCl-0.075. c-g) HAADF-STEM image with elemental mappings of $Co(OH)_2$/CNTs-IrCl-0.075. (Ir centers were highlighted in red circles). (For interpretation of the references to colour in this figure legend, the reader is referred to the web version of this article).

structure parameters, such as coordination number (CN), bond distance (R), and Debye-Waller factor on the absorbing atoms, were permitted to be changed in a fitting process. The range of $k = 3$—11 Å^{-1} ($R = 1.0$—2.5 Å (k^3 weighted)) was chosen as the fitted regions in k and R spaces.

3. Results and discussion

Fig. 1a presents a schematic cartoon procedure for the *in-situ* atomic dispersing $IrCl_x$ on the surfaces of ultrathin $Co(OH)_2$ via facile synthetic strategy at ambient temperature. In this typical process, $IrCl_3·xH_2O$ was directly added into the aqueous solution containing $Co(OH)_2$/CNTs. A series of catalysts of $Co(OH)_2$/CNTs-IrCl-x (x = 0, 0.05, 0.075, 0.15) were obtained with stirring for 6 h by varying the feeding amount of $IrCl_3$. As shown in Fig. 1b and Figs. S1-S5, the TEM and SEM images of $Co(OH)_2$/CNTs-IrCl-x (x = 0, 0.05, 0.075, 0.15) show that the $Co(OH)_2$ exhibits ultrathin nanosheet-like structure, which was homogeneously distributed around the CNTs. The $Co(OH)_2$/CNTs-IrCl-0.075 sample was selected as a model for detail characterization. The HAADF-STEM image definitely shows that abundant of iridium centers are uniformly dispersed on the $Co(OH)_2$/CNTs nanohybrids (Fig. 1c) without Ir-based particles or grains on the ultrathin nanosheets. These results are also confirmed by XRD results (Fig. S6) in which no diffraction signals of Ir-based particles are detected. However, when the concentration ratio of $IrCl_3·H_2O$ and $Co(OH)_2$/CNTs was further increased to 0.15, the $IrCl_x$ clusters with the size of $1 - 2$ nm have even distribution on the surfaces of the $Co(OH)_2$ nanosheets. The selected area electron diffraction (SAED) pattern (inset of Fig. S7a) shows $Co(OH)_2$ is polycrystalline. No obvious lattice fringes of $IrCl_x$ clusters can be observed, suggesting their amorphous nature (Fig. S7). Elemental mapping analysis demonstrates the homogeneous distribution of Co, O and Ir in this single-molecule catalyst (Fig. 1d–g). The loading content of Ir was determined to be ~3.4 wt% by ICP-MS.

The detailed surface states of the as-prepared samples have also been identified by XPS. According to the Ir 4f spectra, the fitting curves are exactly the same no matter what the Ir content varied. XPS spectra (Fig. S8) of Ir reference materials (Ir, $IrCl_3$ and IrO_2) have also been done, including the binding energy signals for Ir (Ir $4f_{7/2}$ 60.8 eV, Ir $4f_{5/2}$ 63.8 eV), IrO_2 (Ir $4f_{7/2}$ 61.9 eV, Ir $4f_{5/2}$ 64.9 eV), and $IrCl_3·xH_2O$ ($4f_{7/2}$ 62.6 eV, $4f_{5/2}$ 65.6 eV). Fig. 2a shows that the binding energies of Ir 4f for $Co(OH)_2$/CNTs-IrCl-x close to that of IrO_2 reference, indicating its full Ir(IV) oxidation state. Furthermore, the binding energies of the Ir $4f_{7/2}$ and $4f_{5/2}$ have positive shift of ~0.7 eV. This shift is caused by the electronic interaction between $IrCl_x$ and $Co(OH)_2$ nanosheets. The absence of peak related to Ir° hints that only molecular Ir-Cl species instead of Ir-based particles/grains in the $Co(OH)_2$/CNTs-IrCl-0.05 and $Co(OH)_2$/CNTs-IrCl-0.075 samples [41], which is consistent with the analyses of XRD and TEM. For $Co(OH)_2$/CNTs-IrCl-0.15, the binding energy of Ir $4f_{7/2}$ shifts negatively (0.2 eV) to 61.0 eV compared to that of above two samples, and more positive than that of Ir° $4f_{7/2}$ (60.8 eV), which can be attributed to the formation of Ir-based clusters/nanoparticles in $Co(OH)_2$/CNTs-IrCl-0.15 with increasing the loading amount of $IrCl_3$. High-resolution Co 2p spectra revealing two main peaks about 781.1 and 797.1 eV and both satellite-peaks can be indexed to the typical signals for Co $2p_{3/2}$ and Co $2p_{1/2}$ orbitals (Figs. 2b, S9), respectively, fitting well with Co^{2+} state in α-$Co(OH)_2$ [42]. The O 1s spectra of $Co(OH)_2$/CNTs-IrCl-x at 531.7 eV can be split into two peaks for oxygen defect species and 532.9 eV for hydroxyl radicals [43], respectively, suggesting the oxygen vacancy in the structure (Fig. S10).

The local structures of Ir species in the atomic-dispersed catalyst of $Co(OH)_2$/CNTs-IrCl-0.075 were further investigated by EXAFS and XANES. The EXAFS fitting results (Fig. 2c and Table S1) show a strong peak at 2.34 Å with coordination number (CN) of 5.7, which was identified for the contribution from Ir-Cl shell compared to that of $IrCl_3$

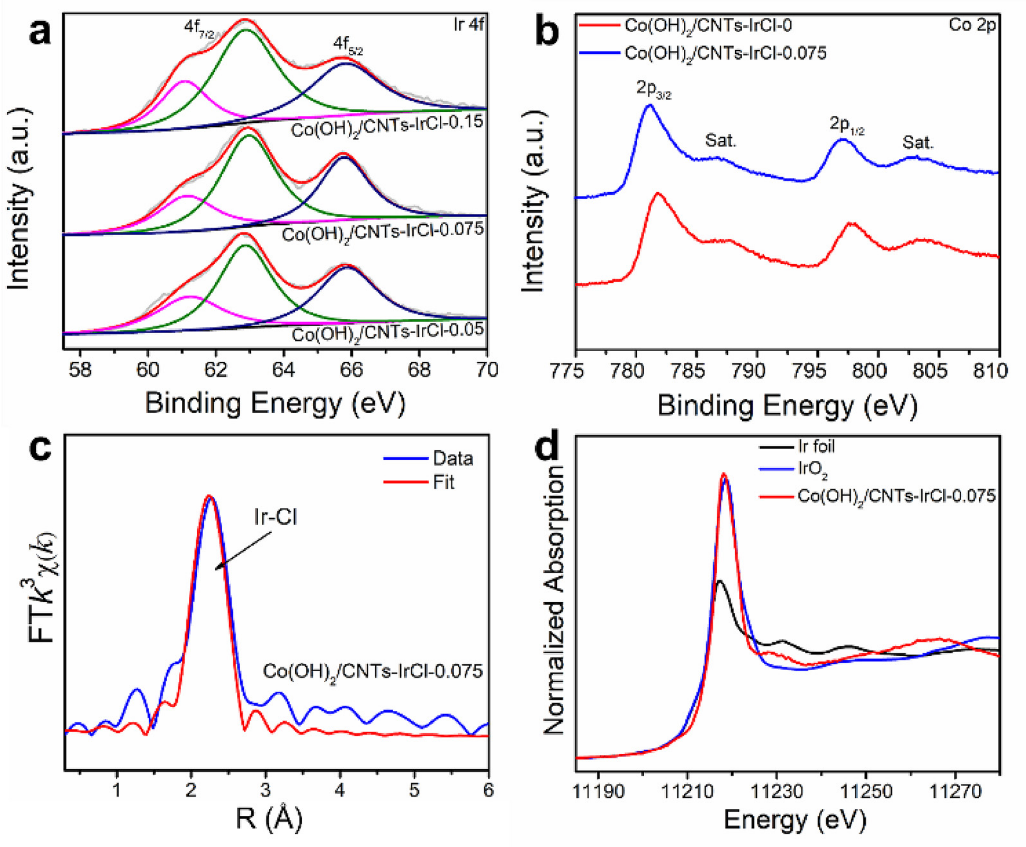

Fig. 2. XPS of a) Ir 4f and b) Co 2p regions of $Co(OH)_2$/CNTs-IrCl-x. c) Ir L_3-edge EXAFS and, d) XANES of $Co(OH)_2$/CNTs-IrCl-0.075 and Ir foil standard.

reference, attributed by the scattering iridium-chloride species. Besides, the other contribution from Ir-O shell (reference: IrO_2) can also be verified during the fit (2.00 Å, CN = 1.2). No obvious Ir-Ir or Ir-Co scattering peaks can be detected, confirming the atomic dispersion of iridium centers, and each iridium center is surrounded by six anions, resulting in $IrCl_6$ in the form of Ir-Cl-Co bridge bonds, and Cl_5-Ir-O bond in the form of Cl-Ir-O mode. In addition, the oxidation state of Ir has been determined by the XANES. The absorption edge energy of $Co(OH)_2$/CNTs-IrCl-0.075 is similar to that of IrO_2, which further reveals the full oxidation state of Ir(IV).

DFT calculations were further conducted to provide deep understanding of the activity of the $IrCl_x$ decorating $Co(OH)_2$ towards OER. The planes of (001) and (110) in $Co(OH)_2$ were chosen as the representative surfaces. This is mainly because that these facets are the most commonly used crystal surfaces with high catalytic activity in the related two-dimensional materials [45, 46]. These two surfaces together can comprehensively investigate the different possible active sites on the catalyst. The charge density differences, total and PDOS, and Mulliken charge analysis have been considered for paving the electronic states of the samples (Figs. 3, S12, and S13). As shown in Fig. 3c, taking $Co(OH)_2$-$IrCl_5$ as an example, the bonding Co 3d with O 2p is responding for the occupied states under Fermi level. It can be seen that Co 3d occupied a higher state energy beyond −4 eV, which is for $3d^7$ high spin state. This implies the oxidation state of Co^{2+}. The $Co(OH)_2$ and $IrCl_5$-$Co(OH)_2$ systems show band gaps with values of 0.27 and 0.07 eV, respectively. This is mainly attributed to the electron transfer between single-molecule $IrCl_5$ and $Co(OH)_2$ substrate (Fig. 3b). Thus the much boosted OER performance over $IrCl_5$ decorating $Co(OH)_2$ could be ascribed to the relative small band gap with strong electronic conductivity [47]. More charges transfer from absorbed O in deprotonation step (from *OH to *O), which leads to lower potential limiting step and higher OER activity [48]. Furthermore, previous studies indicate that free energy for O* with respect to OH* is the main factor to determine OER activity. As illustrated in Fig. 3d, the plot of OER activity versus (ΔG (O*) − ΔG (OH*)) exhibits a feature of shaped volcano [49], where the OER activity is approaching the peak when $IrCl_5$ anchored to the surfaces of $Co(OH)_2$ nanosheets. In addition, DFT study of the O, Ir active sites on different facets of $Co(OH)_2$ and CoOOH catalysts are also given in Fig. 3a and Tables S3-S6, where the Ir atoms are almost in a saturated state over which OER cannot occur. The results show that the O active sites on Ir-contained surfaces have better activity than that of pure $Co(OH)_2$ or CoOOH catalysts. Moreover, the DFT calculations of the $IrCl_6$ decorating $Co(OH)_2$ toward OER were also conducted (Fig. S13). The band gap of $IrCl_6$-$Co(OH)_2$ is decreased to 0.013 eV in comparison with bare $Co(OH)_2$, indicating its enhanced conductivity. Therefore, the strong interfacial electronic interaction between $IrCl_x$ molecules and $Co(OH)_2$ nanosheets enables $Co(OH)_2$/CNTs-$IrCl_x$ to be efficient electrocatalysts to drive OER.

The catalytic OER performance of $Co(OH)_2$/CNTs-$IrCl_x$ was evaluated in aqueous solution of 1 M KOH. For comparisons, $Co(OH)_2$, $Co(OH)_2$/CNTs, IrCl-$Co(OH)_2$, $Co(OH)_2$/CNTs-IrCl-x and IrO_2 were evaluated concurrently under the same condition. Firstly, the activities of $Co(OH)_2$/CNTs at various contents of CNTs have been studied. Fig. S14 (Supporting information) shows that the CNTs are very important to enhance the electrochemical performance. When increasing quantity of CNTs to 2.5 mg, the $Co(OH)_2$/CNTs shows the best performance with the overpotential of 308 mV, which is much less than those over $Co(OH)_2$/CNTs-1.5 mg (401 mV) and $Co(OH)_2$/CNTs-5 mg (315 mV), respectively. Additionally, LSV curves (Figs. 4a and S15) scanned at 10 mV s^{-1} show that the $Co(OH)_2$/CNTs-IrCl-0.075 exhibits the highest OER activity among these detected catalysts, where the overpotentials (η) at a current density (j) of 10 mA cm^{-2} are 340 mV for $Co(OH)_2$, 309 mV for IrO_2, 308 mV for $Co(OH)_2$/CNTs, 299 mV for $Co(OH)_2$-IrCl-0.075 and 230 mV for $Co(OH)_2$/CNTs-IrCl-0.075, respectively, hinting

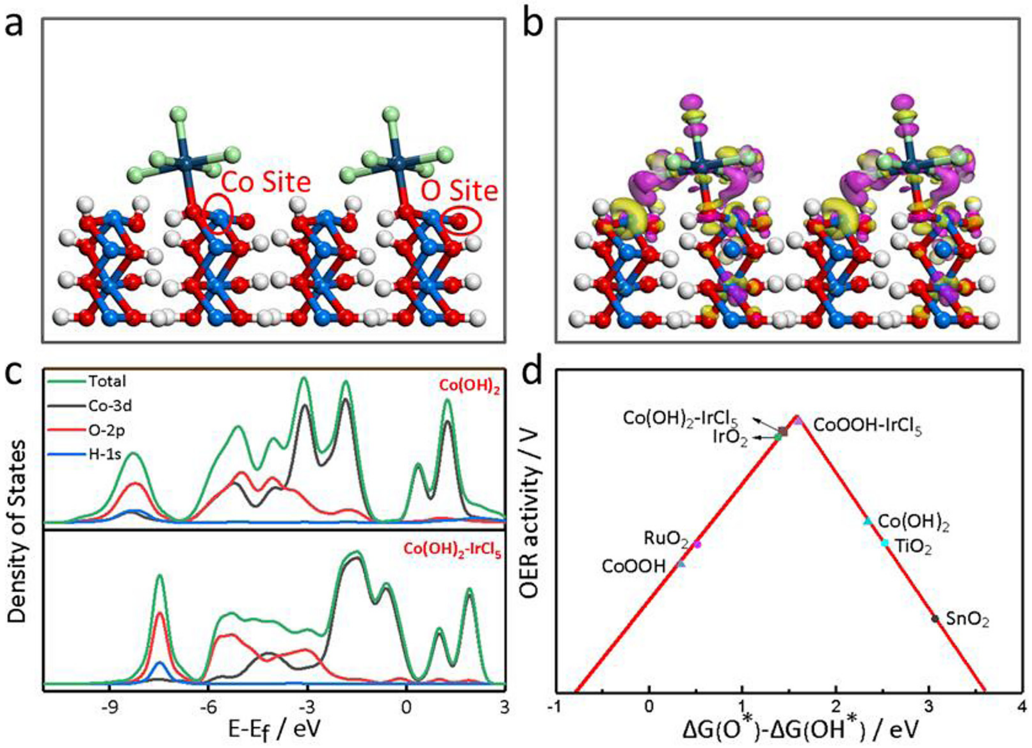

Fig. 3. a) Optimized geometric structure and b) the charge density discrepancy between $Co(OH)_2$ and $Co(OH)_2$-$IrCl_5$, where the yellow and pink colors are for the charge depletion and charge accumulation, respectively. c) DOS for $Co(OH)_2$ and $Co(OH)_2$-$IrCl_5$. d) Plot of Activity trends towards OER versus ΔG (O*) − ΔG (OH*) (the values of RuO_2, TiO_2 and SnO_2 w the values of IrO_2 were taken from ref. [44]. (For interpretation of the references to colour in this figure legend, the reader is referred to the web version of this article).

that the atomic Ir-Cl species are conductive to enhance the OER performance of $Co(OH)_2$/CNTs-IrCl-0.075. The values are also better than mostly reported data of transition metal-based eletrocatalysts (Table S2). The CV curves were also used to estimate the OER activity of the as-prepared electrocatalysts, in which the $Co(OH)_2$/CNTs-IrCl-0.075 and $Co(OH)_2$/CNTs-IrCl-0.15 exhibit larger *j* and earlier onset of *j* compared to the $Co(OH)_2$/CNTs with other compositions, which matched the LSV results (Figs. S16 and S18). The Tafel slopes of $Co(OH)_2$, IrO_2, $Co(OH)_2$/CNTs, $Co(OH)_2$-IrCl-0.075, and $Co(OH)_2$/CNTs-IrCl-0.075 are determined to be 168.88, 96.61, 114.10, 92.83 and 71.64 mV dec^{-1}, respectively (Fig. 4b, S17). The lowest Tafel slope value of the $Co(OH)_2$/CNTs-IrCl-0.075 sample indicates a faster reaction kinetics and a lower energy consumption in electrochemical processes. In order to understand the excellent OER performance of $Co(OH)_2$/CNTs-IrCl-0.075, we also measured the values of C_{dl} (Fig. 4c, d). The C_{dl} values of $Co(OH)_2$/CNTs-IrCl-0, $Co(OH)_2$/CNTs-IrCl-0.05, $Co(OH)_2$/CNTs-IrCl-0.075 and $Co(OH)_2$/CNTs-IrCl-0.15 are determined to be 17.8, 27.65, 54.9 and 23.1 m F cm^{-2}, respectively (Figs. S19-S21), and the ESCA values of the $Co(OH)_2$/CNTs-IrCl-x (x = 0, 0.05, 0.075, 0.15) are 31.15 cm^{-2}, 48.39 cm^{-2}, 96.08 cm^{-2}, 40.43 cm^{-2}, respectively, demonstrating that $Co(OH)_2$/CNTs-IrCl-0.075 has the highest electrochemical specific surface area, ESCA with exposed more active sites. Herein, the intrinsic activity of electrocatalysts normalized ECSA was also performed (Fig. S22). The results further indicate that the catalytic activity is greatly improved after loading $IrCl_x$, among which the single-molecule dispersed $IrCl_x$ facilitates the best performance. Fig. 4e is the electrochemical impedance spectroscopy (EIS) of the sample, which is often used to probe into electron-transfer capacity of the electrocatalysts. It is showing the conductivity of $Co(OH)_2$/CNTs has been improved after adding the CNTs in comparison wtih $Co(OH)_2$. The $Co(OH)_2$/CNTs-IrCl-0.075 exhibits the highest conductivity, suggesting the molecular Ir-Cl species are beneficial for the electron transfer and improving the catalytic performance (Fig. S23). Moreover, as illustrated in Fig. 4f, the $Co(OH)_2$/CNTs-IrCl-0.075 displays good durability in alkaline solution even after the reaction continued for 24 h in amperometric measurement at a potential of 1.48 V. Furthermore, we carried out cycling tests over all the catalysts. As shown in Figures S16, S17, the recovered $Co(OH)_2$/CNTs-IrCl-0.075 catalyst still retained a very high OER performance even after 2000 cycles. The HAADF-STEM image of $Co(OH)_2$/CNTs-IrCl-0.075 after the amperometric test shows the atomic dispersion of Ir centers on the ultrathin nanosheets still maintained (Fig. S24), further proving the excellent stability of the title catalysts. The ICP analysis of the electrolyte after the tests shows no Ir species dissolved in the electrolyte. XPS spectra of the product after cycling (Fig. S25) reveal a spin-orbit level energy spacing of 15 eV vs 16 eV over the catalyst, implying that the transformation of Co^{II} to Co^{III} occurs. The case is common during the OER reaction, where conversion of $Co(OH)_2$ to $Co^{III}O_x(OH)$ dominates key step for the oxygen evolution [50]. The binding energy peaks of the $IrCl_x$ $4f_{7/2}$, and $IrCl_x$ $4f_{5/2}$ have no obvious valence changes over $IrCl_x$ species, further indicating they are stable during the cycling reactions.

4. Conclusion

In summary, a facile strategy to construct single-molecule catalysts by utilizing ultrathin $Co(OH)_2$/CNTs nanosheets to immobilize $IrCl_x$ molecules has been developed to produce atomically-dispersed hybridized electrocatalysts. Engineering the surface of the flexible ultrathin substrate with single-molecule $IrCl_x$ via the Ir-Cl-Co bonds and Ir-O-Co makes the single-molecule catalysts possess strong electronic interaction and excellent charge transfer capability, which greatly contributed to the efficient OER activity. The $Co(OH)_2$/CNTs-IrCl-0.075 exhibits an overpotential of 230 mV at 10 mA cm^{-2} and corresponding Tafel slope of 71.64 mV dec^{-1}, which was enhanced compared to that over pristine $Co(OH)_2$/CNTs and commercial IrO_2. Theoretical calculations indicate that single-molecule $IrCl_x$ species-decorating $Co(OH)_2$ can significantly enhance the interfacial electron transfer to create oxygen active sites in $Co(OH)_2$-$IrCl_x$ with more positive charge. Thus, it can efficiently derive OER by facilely capturing electrons from water molecules. This work will provide a facile method to fabricate transition-metal oxide/hydroxide supported single-molecule catalyst for various specific applications, and a good model to study the detailed structure-performance relationship on the atomic scale.

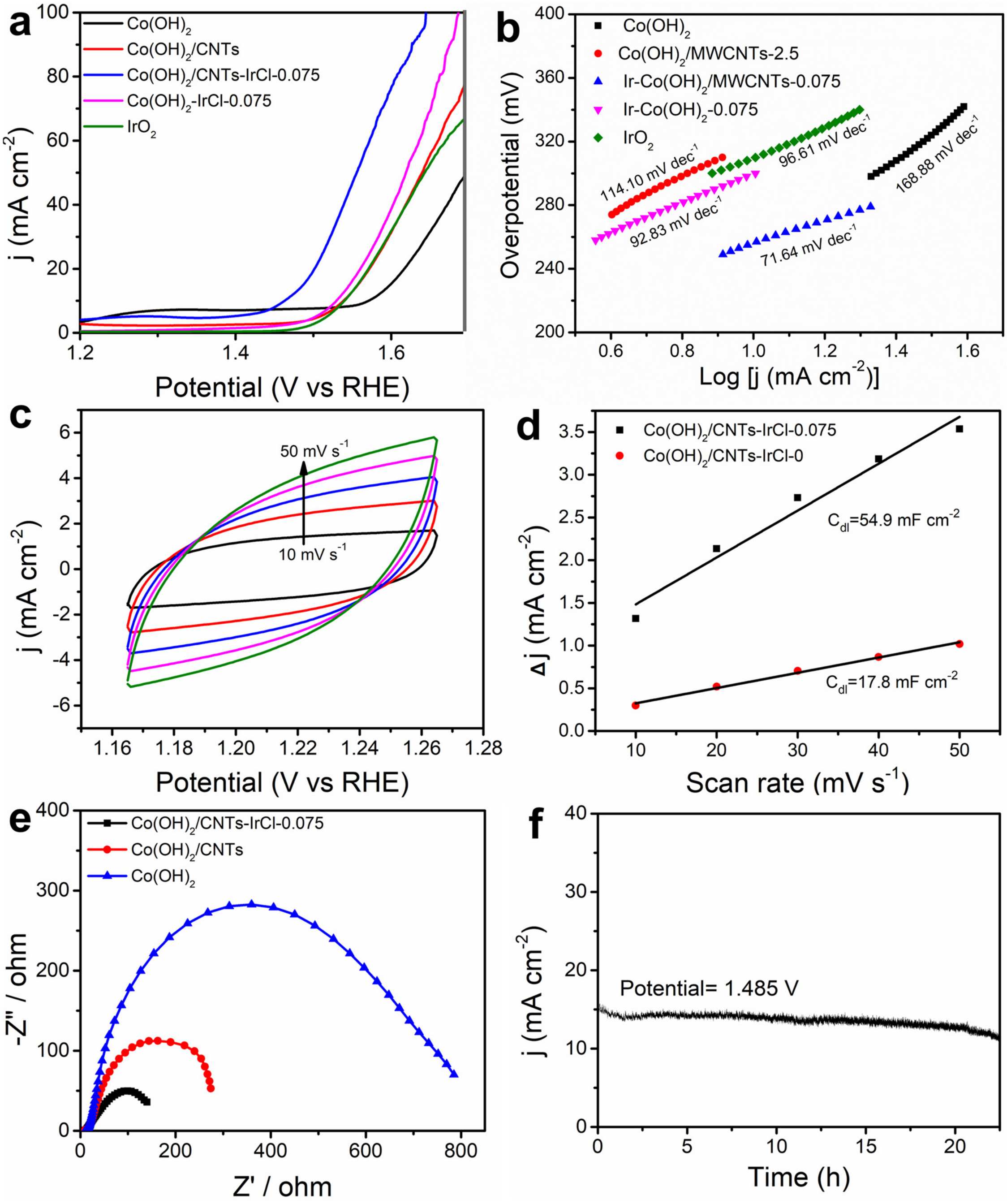

Fig. 4. a) LSV curves, b) Tafel slopes of the as-prepared samples and IrO_2, and c) CVs scanning over $Co(OH)_2$/CNTs-IrCl-0.075 with a rate of 10 - 50 mV/s and d) the plot of capacitive currents vs scan rates at 1.22 V, e) Nyquist plots of $Co(OH)_2$, $Co(OH)_2$/CNTs, $Co(OH)_2$/CNTs-IrCl-0.075 at 1.525 V (vs. RHE), f) Current density over Time at 1.485 V for $Co(OH)_2$/CNTs-IrCl-0.075.

CRediT authorship contribution statement

Yiwen Huang: Conceptualization, Investigation, Data curation, Writing - original draft. **Guijuan Wei:** Data curation, Writing - original draft. **Jia He:** Investigation, Formal analysis, Software. **Cuihua An:** Writing - review & editing, Formal analysis. **Min Hu:** Investigation, Formal analysis. **Miao Shu:** Resources, Data curation. **Junfa Zhu:** Resources, Data curation. **Shuang Yao:** Writing - review & editing, Investigation. **Wei Xi:** Resources, Data curation. **Rui Si:** Resources, Data curation, Formal analysis. **Zhi-Ming Zhang:** Writing - review & editing, Investigation. **Changhua An:** Conceptualization, Methodology, Supervision, Project administration, Funding acquisition.

Declaration of Competing Interest

The authors claim no competing financial interest.

Acknowledgments

This work is supported by the National Natural Science Foundation of China (21771137, 21773288 and 21722104), Natural Science Foundation of Tianjin City of China (18JCJQJC47700).

Appendix A. Supplementary data

Supplementary material related to this article can be found, in the online version, at doi:https://doi.org/10.1016/j.apcatb.2020.119398.

References

[1] S. Chu, A. Majumdar, Opportunities and challenges for a sustainable energy future, Nature 488 (2012) 294–303 https://www.nature.com/articles/nature11475.

[2] G. Liu, P. Li, G. Zhao, X. Wang, J. Kong, H. Liu, H. Zhang, K. Chang, X. Meng, T. Kako, Promoting active species generation by plasmon-induced hot-electron excitation for efficient electrocatalytic oxygen evolution, J. Am. Chem. Soc. 138 (2016) 9128–9136, https://doi.org/10.1021/jacs.6b05190.

[3] K. Motokura, D. Nishimura, K. Mori, T. Mizugaki, K. Ebitani, K. Kaneda, A ruthenium-grafted hydrotalcite as a multifunctional catalyst for direct α-alkylation of nitriles with primary alcohols, J. Am. Chem. Soc. 18 (2004) 5662–5663, https://doi.org/10.1021/ja049181l.

[4] K. Motokura, N. Fujita, Mori K. Kohsuke, T. Mizugaki, K. Kohki Ebitani, K. Jitsukawa, K. Kaneda, Environmentally friendly one pot synthesis of α-alkylated nitriles using hydrotalcite-supported metal species as multifunctional solid catalysts, Chem. Eur. J. 12 (2006) 8228–8239, https://doi.org/10.1002/chem.200600317.

[5] K. Mori, T. Taga, H. Yamashita, Isolated single-atomic Ru catalyst bound on a layered double hydroxide for hydrogenation of CO_2 to formic acid, ACS Catal. 5 (2017) 3147–3151, https://doi.org/10.1021/acscatal.7b00312.

[6] Y. Pi, Q. Shao, P. Wang, F. Lv, S. Guo, J. Guo, X. Huang, Trimetallic oxyhydroxide coralloids for efficient oxygen evolution electrocatalysis, Angew. Chem. Int. Ed. 56 (2017) 4502–4506, https://doi.org/10.1002/anie.201701533.

[7] A. Wu, Y. Xie, H. Ma, C. Tian, Y. Gu, H. Yan, X. Zhang, G. Yang, H. Fu, Integrating the active OER and HER components as the heterostructures for the efficient overall water splitting, Nano Energy 44 (2018) 353–363, https://doi.org/10.1016/j.nanoen.2017.11.045.

[8] H.Y. Wang, S.F. Hung, H.Y. Chen, T.S. Chan, H.M. Chen, B. Liu, In operando identification of geometrical-site-dependent water oxidation activity of spinel Co_3O_4, J. Am. Chem. Soc. 138 (2015) 36–39, https://doi.org/10.1021/jacs.5b10525.

[9] B. Zhang, X. Zheng, O. Voznyy, R. Comin, M. Bajdich, M. García-Melchor, L. Han, J. Xu, M. Liu, L. Zheng, Homogeneously dispersed multimetal oxygen-evolving catalysts, Science 352 (2016) 333–337 https://science.sciencemag.org/content/352/6283/333.

[10] Z.W. Seh, J. Kibsgaard, C.F. Dickens, I. Chorkendorff, J.K. Nørskov, T.F. Jaramillo, Combining theory and experiment in electrocatalysis: insights into materials design, Science 355 (2017) 4998–5012 http://science.sciencemag.org/content/355/6321/eaad4998.

[11] M.B. Stevens, L.J. Enman, A.S. Batchellor, M.R. Cosby, A.E. Vise, C.D. Trang, S.W. Boettcher, Measurement techniques for the study of thin film heterogeneous water oxidation electrocatalysts, Chem. Mater. 29 (2016) 120–140, https://doi.org/10.1021/acs.chemmater.6b02796.

[12] B. Li, S. Chen, J. Tian, M. Gong, H. Xu, L. Song, Amorphous nickel-iron oxides/carbon nanohybrids for an efficient and durable oxygen evolution reaction, Nano Res. 10 (2017) 3629–3637, https://doi.org/10.1007/s12274-017-1572-9.

[13] X. Yan, Y. Jia, J. Chen, Z. Zhu, X. Yao, Defective-activated-carbon-supported Mn-Co-nanoparticles as a highly efficient electrocatalyst for oxygen reduction, Adv. Mater. 28 (2016) 8771–8778, https://doi.org/10.1002/adma.201601651.

[14] L. Xu, Q. Jiang, Z. Xiao, X. Li, J. Huo, S. Wang, L. Dai, Plasma-engraved Co_3O_4 nanosheets with oxygen vacancies and high surface area for the oxygen evolution reaction, Angew. Chem. Int. Ed. 55 (2016) 5277–5281, https://doi.org/10.1002/ange.201600687.

[15] Y. Jiao, Y. Zheng, M. Jaroniec, S.Z. Qiao, Design of electrocatalysts for oxygen-and hydrogen-involving energy conversion reactions, Chem. Soc. Rev. 44 (2015) 2060–2086, https://doi.org/10.1039/C4CS00470A.

[16] H. Wang, H.W. Lee, Y. Deng, Z. Lu, P.C. Hsu, Y. Liu, D. Lin, Y. Cui, Bifunctional non-noble metal oxide nanoparticle electrocatalysts through lithium-induced conversion for overall water splitting, Nat. Commun. (2015) 67261–67269 http://www.nature.com/articles/ncomms8261.pdf.

[17] Q.Q. Chen, C.C. Hou, C.J. Wang, X. Yang, R. Shia, Y. Chen, Ir^{4+}-Doped NiFe LDH to expedite hydrogen evolution kinetics as a Pt-like electrocatalyst for water splitting, Chem. Commun. 54 (2018) 6400–6403, https://doi.org/10.1039/C8CC02872A.

[18] G.B. Chen, T. Wang, J. Zhang, P. Liu, H.J. Sun, X.D. Zhuang, M.W. Chen, X.L. Feng, Accelerated hydrogen evolution kinetics on NiFe-layered double hydroxide electrocatalysts by tailoring water dissociation active sites, Adv. Mater. 30 (2018) 1706279, , https://doi.org/10.1002/adma.201706279.

[19] T.Y. Ma, S. Dai, M. Jaroniec, S.Z. Qiao, Graphitic carbon nitride nanosheet-carbon nanotube three-dimensional porous composites as high-performance oxygen evolution electrocatalysts, Angew. Chem. Int. Ed. 53 (2014) 7281–7285, https://doi.org/10.1002/anie.201403946.

[20] Z. Xue, X. Li, Q. Liu, M. Cai, K. Liu, M. Liu, Z. Ke, X. Liu, G. Li, Interfacial electronic structure modulation of NiTe nanoarrays with NiS nanodots facilitates electrocatalytic oxygen evolution, Adv. Mater. 31 (2019) 1900430, , https://doi.org/10.1002/adma.201900430.

[21] M. Kuang, P. Han, L. Huang, N. Cao, L. Qian, G. Zheng, Electronic tuning of Co, Ni based nanostructured (Hydr) oxides for aqueous electrocatalysis, Adv. Funct. Mater. 28 (2018) 1804886, , https://doi.org/10.1002/adfm.201804886.

[22] Y. Bi, Z. Cai, D. Zhou, Y. Tian, Y. Kuang, Y. Li, X. Sun, X. Duan, Understanding the incorporating effect of Co^{2+}/Co^{3+} in NiFe-layered double hydroxide for electrocatalytic oxygen evolution reaction, J. Catal. 358 (2018) 100–107, https://doi.org/10.1016/j.jcat.2017.11.028.

[23] P. He, X.Y. Yu, X.W. Lou, Carbon incorporated nickel-cobalt mixed metal phosphide nanoboxes with enhanced electrocatalytic activity for oxygen evolution, Angew. Chem. Int. Ed. 56 (2017) 3897–3900, https://doi.org/10.1002/anie.201612635.

[24] X. Wang, T. Ouyang, L. Wang, J. Zhong, T. Ma, Z. Liu, Redox-inert Fe^{3+} in octahedral sites of Co-Fe spinel oxides with enhanced oxygen catalytic activity for rechargeable Zn-air batteries, Angew. Chem. Int. Ed. 38 (2019) 13425–13430, https://doi.org/10.1002/ange.201907595.

[25] Y. Zhang, C. Wu, H. Jiang, Y. Lin, H. Liu, Q. He, S. Chen, T. Duan, L. Song, Atomic Iridium incorporated in cobalt hydroxide for efficient oxygent evolution catalysis in nertral electrolyte, Adv. Mater. 30 (2018) 1707522, , https://doi.org/10.1002/adma.201707522.

[26] X. Wang, T. Ouyang, L. Wang, J. Zhong, Z. Liu, Surface reorganization on electrochemically-induced Zn-Ni-Co spinel oxides for enhanced oxygen electrocatalysis, Angew. Chem. Int. Ed. 16 (2020) 6554–6561, https://doi.org/10.1002/ange.202000690.

[27] N. Du, C. Wang, X. Wang, Y. Lin, J. Jiang, Y. Xiong, Trimetallic tristar nanostructures: tuning electronic and surface structures for enhanced electrocatalytic hydrogen evolution, Adv. Mater. 28 (2016) 2077–2084, https://doi.org/10.1002/adma.201504785.

[28] Y. Sun, S. Gao, F. Lei, Y. Xie, Atomically-thin two-dimensional sheets for understanding active sites in catalysis, Chem. Soc. Rev. 44 (2015) 623–636, https://doi.org/10.1039/C4CS00236A.

[29] M. Blasco-Ahicart, J. Soriano-López, J.J. Carbó, J.M. Poblet, J. Galan-Mascaros, Polyoxometalate electrocatalysts based on earth-abundant metals for efficient water oxidation in acidic media, Nat. Chem. 10 (2018) 24–30 https://www.nature.com/articles/nchem.2874.pdf.

[30] H. Tang, J. Wei, F. Liu, B. Qiao, X. Pan, L. Li, J. Liu, J. Wang, T. Zhang, Strong metal-support interactions between gold nanoparticles and nonoxides, J. Am. Chem. Soc. 138 (2015) 56–59, https://doi.org/10.1021/jacs.5b11306.

[31] J. Zhang, H. Wang, L. Wang, S. Ali, C. Wang, L. Wang, X. Meng, B. Li, D.S. Su, F.S. Xiao, Wet-chemistry strong metal-support interactions in titania supported Au catalysts, J. Am. Chem. Soc. 141 (2019) 2975–2983, https://doi.org/10.1021/jacs.8b10864.

[32] Q. Fu, T. Wagner, Metal/oxide interfacial reactions: Oxidation of metals on $SrTiO_3$ (100) and TiO_2 (110), J. Phys. Chem. B 10 (2005) 911697–911705, https://doi.org/10.1021/jp050601i.

[33] E.I. Solomon, P.M. Jones, J.A. May, Electronic structures of active sites on metal oxide surfaces: definition of the copper-zinc oxide methanol synthesis catalyst by photoelectron spectroscopy, Chem. Rev. 93 (1993) 2623–2644, https://doi.org/10.1021/cr00024a003.

[34] P. Hu, Z. Huang, Z. Amghouz, M. Makkee, F. Xu, F. Kapteijn, A. Dikhtiarenko, Y. Chen, X. Gu, X. Tang, Electronic metal-support interactions in single-atom catalysts, Angew. Chem. Int. Ed. 53 (2014) 3418–3421, https://doi.org/10.1002/ange.201309248.

[35] F. Shi, L.R. Baker, A. Hervier, G.A. Somorjai, K. Komvopoulos, Tuning the electronic structure of titanium oxide support to enhance the electrochemical activity of platinum nanoparticles, Nano Lett. 13 (2013) 4469–4474, https://doi.org/10.1021/nl402392u.

[36] J. Huang, J. Chen, T. Yao, J. He, S. Jiang, Z. Sun, Q. Liu, W. Cheng, F. Hu, Y. Jiang, CoOOH nanosheets with high mass activity for water oxidation, Angew. Chem. Int. Ed. 54 (2015) 8722–8727, https://doi.org/10.1002/ange.201502836.

[37] J.P. Perdew, K. Burke, M. Ernzerhof, Generalized gradient approximation made simple, Phys. Rev. Lett. 18 (1996) 3865, , https://doi.org/10.1103/PhysRevLett.77.3865.

[38] B. Delley, From molecules to solids with the DMol3 approach, J. Chem. Phys. 7756 (2000) 7756–7764, https://doi.org/10.1063/1.1316015.

[39] L. Feng, Y. Liu, J. Zhao, Fe-and Co-P 4-embedded graphenes as electrocatalysts for the oxygen reduction reaction: theoretical insights, Phys. Chem. Chem. Phys. 45 (2015) 30687–30694, https://doi.org/10.1039/C5CP05551B.

[40] A.I. Frenkel, Q. Wang, N. Marinkovic, J.G. Chen, L. Barrio, R. Si, A.L. Camara, A.M.J. Estrella, A. Rodriguez, J.C. Hanson, Combining X-ray absorption and X-ray diffraction techniques for in situ studies of chemical transformations in heterogeneous catalysis: advantages and limitations, J. Phys. Chem. C 36 (2011) 17884–17890, https://doi.org/10.1021/jp205204e.

[41] B. El-Issa, A. Katrib, R. Ghodsian, B. Salsa', S. Addassi, A comparative study of the bonding in different halides of iridium, Int. J. Quantum Chem. Quantum Biol. Symp. 33 (1988) 195–216, https://doi.org/10.1002/qua.560330305.

[42] T. Xue, X. Wang, J.M. Lee, Dual-template synthesis of $Co(OH)_2$ with mesoporous nanowire structure and its application in supercapacitor, J. Power Sources 201 (2012) 382–386, https://doi.org/10.1016/j.jpowsour.2011.10.138.

[43] A. Frenkel, Q. Wang, N. Marinkovic, J. Chen, L. Barrio, R. Si, A.L. Cámara, A. Estrella, J. Rodriguez, J. Hanson, Combining X-ray absorption and X-ray diffraction techniques for in situ studies of chemical transformations in heterogeneous catalysis: advantages and limitations, J. Phys. Chem. C 115 (2011) 17884–17890, https://doi.org/10.1021/jp205204e.

[44] G. Liu, P. Li, G. Zhao, X. Wang, J. Kong, H. Liu, H. Zhang, K. Chang, X. Meng, T. Kako, Promoting active species generation by plasmon-induced hot-electron excitation for efficient electrocatalytic oxygen evolution, J. Am. Chem. Soc. 138 (2016) 9128–9136, https://doi.org/10.1021/jacs.6b05190.

[45] X. Zhao, X. Xiong, X. Duan, Y. Xu, Y. Li, First-principles study of oxygen evolution reaction on Ni3Fe-layered double hydroxides surface with different oxygen coverage, Mol. Catal. 490 (2020) 110957, , https://doi.org/10.1016/j.mcat.2020.110957.

[46] Y. Bi, Z. Cai, D. Zhou, Y. Tian, Q. Zhang, Q. Zhang, Y. Kuang, Y. Li, X. Sun, X. Duan, Understanding the incorporating effect of Co^{2+}/Co^{3+} in NiFe-layered double hydroxide for electrocatalytic oxygen evolution reaction, J. Catal. 358 (2018) 100–107, https://doi.org/10.1016/j.jcat.2017.11.028.

[47] K. Yang, P. Xu, Z. Lin, Y. Yang, P. Jiang, C. Wang, S. Liu, S. Gong, L. Hu, Q. Chen, Ultrasmall Ru/Cu doped RuO_2 complex embedded in amorphous carbon skeleton as highly active bifunctional electrocatalysts for overall water splitting, Small 14 (2018) 1803009, , https://doi.org/10.1002/smll.201803009.

[48] Y. Bi, Z. Cai, D. Zhou, Y. Tian, Y. Kuang, Y. Li, X. Sun, X. Duan, Understanding the incorporating effect of Co^{2+}/Co^{3+} in NiFe-layered double hydroxide for electrocatalytic oxygen evolution reaction, J. Catal. 358 (2018) 100–107, https://doi.org/10.1016/j.jcat.2017.11.028.

[49] R. Gao, D. Yan, Fast formation of single-unit-cell-thick and defect-rich layered double hydroxide nanosheets with highly enhanced oxygen evolution reaction for water splitting, Nano Res. 11 (2018) 1883–1894, https://doi.org/10.1007/s12274-017-1806-x.

[50] D. McAteer, I. Godwin, Z. Ling, A. Harvey, L. He, C. Boland, V. Mayoral, B. Szydłowska, A. Rovetta, C. Backes, J. Boland, X. Chen, M. Lyons, J. Coleman, Liquid exfoliated $Co(OH)_2$ nanosheets as low-cost, yet high-performance, catalysts for the oxygen evolution reaction, Adv. Energy Mater. 8 (2018) 1702965, , https://doi.org/10.1002/aenm.201702965.